Spectrum of Engineering Sciences
ISSN (e) 3007-3138 (p) 3007-312X Volume 4, Issue 4, 2026

ANALYTICAL SOLUTION OF UNSTEADY STOKES FLOW OF A MAXWELL FLUID WITH TIME-DEPENDENT SLIP IN A POROUS CHANNEL

Younis Ali[*1], Waqas Ahmed Channa[2], Sidra Soomro[3], Faraz Channa[4], Naveed Ahmed[5]

*[*1]Lecturer in Mathematics at Government Islamia Arts and Commerce College Sukkur, Pakistan*
[2]Visiting faculty at the Department of Mathematics, The Shaikh Ayaz University Shikarpur, Sindh, Pakistan
[3]Department of Software Engineering, Mehran University of Engineering & Technology Jamshoro, Sindh Pakistan
[4]Visiting faculty at the Department of Mathematics, The Shaikh Ayaz University Shikarpur, Sindh, Pakistan
[5]Visiting faculty at the Department of Computer Science & IT, The Shaikh Ayaz University Shikarpur, Sindh, Pakistan

[*1]younisalipanhwar@gmail.com, [2]waqaschana222@gmail.com, [3]sidrasoomro14@gmail.com, [4]farazchanna1122@gmail.com, [5]ahmednaveed155@gmail.com

DOI: https://doi.org/10.5281/zenodo.19704260

Keywords
Maxwell fluid; unsteady Stokes flow; porous channel; time-dependent slip; Laplace transform; Darcy number; analytical solution.

Article History
Received: 24 February 2026
Accepted: 04 April 2026
Published: 23 April 2026

Corresponding Author: *
Younis Ali

Abstract

The present article shows an analytical closed form solution for the unsteady Stokes flow of an incompressible Maxwell fluid in a porous parallel plates channel with time dependent Navier slip boundary conditions. The governing partial differential equation is obtained by combining the Maxwell constitutive relation and a Darcy resistance term. The problem is reduced to a second order ordinary differential equation using a Laplace transform approach, and the solution is given in terms of hyperbolic functions. The slip length is defined as $\boldsymbol{\ell(t) = \ell_0(1 + \varepsilon e^{\wedge -\mathrm{it}})}$*, which decays exponentially from an elevated initial value to a constant steady state, modeling progressive surface relaxation. The velocity field is divided into two components: steady-state and exponentially decaying transients. A limiting case analysis aligns with existing Newtonian and no slip solutions. The Stehfest numerical inversion method is verified for accuracy by comparison with finite-difference results. Theoretical analyses indicate that: (i) increasing the dimensionless relaxation time* Λ *slows down the flow development and lowers the maximum velocity; (ii) greater slip leads to a more uniform, plug-like velocity profile; and (iii) reducing the Darcy number diminishes the bulk flow speed. The analytical framework is directly applicable to microfluidic devices, biomedical transport, polymer filtration, and enhanced oil recovery.*

1. INTRODUCTION

The flow of non-Newtonian fluids through confined geometries occupies a central place in modern fluid mechanics, driven by wide-ranging applications in polymer processing, biomedical engineering, enhanced oil recovery, and microfluidics. Among the many rheological models in the literature, the Maxwell fluid model is particularly prominent because it captures viscoelastic relaxation—the ability of the fluid to store and dissipate energy—while remaining analytically tractable [1, 2].

Early work on exact solutions for Maxwell fluids focused on Stokes' first and second problems. Fetecau and Fetecau [3] derived solutions for the first Stokes problem for an Oldroyd-B fluid, which includes the Maxwell model as a special case. Exact solutions for the second Stokes problem (oscillating plate) for Maxwell fluids using the Laplace transform were established by Fetecau et al. [4], who expressed the results as sums of steady-state and transient components. Tan and Masuoka [5] extended this to fractional Maxwell models between parallel plates, demonstrating non-classical diffusion behavior. The Rayleigh–Stokes problem for a Maxwell-type fluid was solved by Shen et al. [6] using Fourier sine transforms.

The presence of a porous medium introduces a Darcy drag that profoundly modifies the flow. Hayat et al. [7] studied MHD boundary-layer flow of an upper convicted Maxwell (UCM) fluid in a porous channel using the homotopy analysis method. Khan et al. [8] obtained exact solutions for MHD flow of a generalized Oldroyd-B fluid in porous media using Laplace and Fourier transforms. Analytical solutions for Maxwell fluid through a porous plate channel driven by an accelerating or oscillating wall were provided by Fetecau et al. [9], using the finite Fourier sine transform; they found that porous medium delays the onset of the steady state. Shah et al. [10] examined fractional Maxwell fluid with second-order slip in a porous medium via the Laplace transform and Stehfest's algorithm. Akhtar et al. [11] treated oscillatory flow of Maxwell fluid in a porous annulus analytically. Mondal et al. [12] studied unsteady MHD periodic flow of a generalized Maxwell fluid through a porous channel.

Ali et al. [13] studied unsteady Stokes flow of a non-Newtonian fluid in a porous channel with periodic suction and injection, providing analytical solutions for velocity distribution under unsteady boundary forcing. However, viscoelastic effects and time-dependent slip conditions were not considered. Therefore, the present study extends this framework by incorporating Maxwell fluid behavior and time-dependent slip boundary conditions in a porous channel.

Velocity slip at solid boundaries is of fundamental importance whenever the continuum no-slip assumption breaks down. This occurs for rarefied gases [1, 15], for polymer melts near walls [14], for flows over super hydrophobic or micro-structured surfaces [15], and in biological micro-channels. The Navier slip model is the simplest and most widely used framework [16, 17]. Khaled and Vafai [18] obtained exact solutions for Stokes and Couette flows of a Newtonian fluid with constant slip using Laplace transforms. Transient flows of Maxwell fluids with constant slip were solved analytically by Vieru and Zafar [19] using the Laplace transform. Pillai and Manu [20] derived analytical solutions for unsteady pipe flows with constant slip. Qi and Liu [21] studied unsteady Poiseuille flow of a second-grade fluid with constant Navier slip, proving well-posedness and obtaining a closed-form series solution.

Despite this body of work, the case of time-dependent slip has received comparatively little analytical attention. Physical situations that motivate a time-varying slip length include progressive surface hydrophilisation or hydrophobisation, temperature- or concentration-dependent wall coatings, and polymer de-wetting during start-up flow. Kaoullas and Georgiou [22] and Damianou et al. [23] considered dynamic slip conditions in the context of viscoplastic fluids in channels, but did not consider viscoelastic fluids or porous media. Corvera Poiré and Hernandez-Machado [24] demonstrated that the apparent slip length of a viscoelastic fluid in a micro channel can change the bulk flow by orders of magnitude under dynamic pressure gradients.

The present work fills this gap by combining, for the first time, (i) Maxwell viscoelasticity, (ii) Darcy porous-medium resistance, and (iii) an exponentially decaying time-dependent slip length of the form $\boldsymbol{\ell(t) = \ell_0(1 + \varepsilon e^{-nt})}$ in a unified analytical framework. The Laplace transform is used to derive a closed-form solution, and the analysis is validated against a finite-difference benchmark. The novelty of the paper resides precisely in the time-dependent slip model within the Maxwell porous-channel setting, a combination not previously treated in the literature.

2. Mathematical Formulation

2.1 Physical Model and Geometry

Consider two infinite, rigid, impermeable parallel plates separated by a gap of width h. The region between the plates, $\mathbf{0} \leq \boldsymbol{y} \leq \boldsymbol{h}$, is completely filled with a homogeneous, isotropic porous medium of uniform porosity $\boldsymbol{\phi}$ and permeability $\boldsymbol{K}$ (Figure 1). The porous skeleton is rigid and stationary; the interconnected pore space is saturated by an incompressible Maxwell viscoelastic fluid of density $\boldsymbol{\rho}$ and dynamic viscosity $\boldsymbol{\mu}$. This configuration models, for example, a packed-bed micro-reactor, a polymer-saturated membrane, or a biological tissue layer confined between two surfaces.

A constant pressure gradient $\boldsymbol{G} = -\boldsymbol{\partial p/\partial x} > \mathbf{0}$ drives the fluid in the x-direction. The flow is assumed to be fully developed, unidirectional, and laminar, so the velocity field reduces to:

$$\boldsymbol{u = u(y, t)\,\check{e}_x} \quad \ldots (1)$$

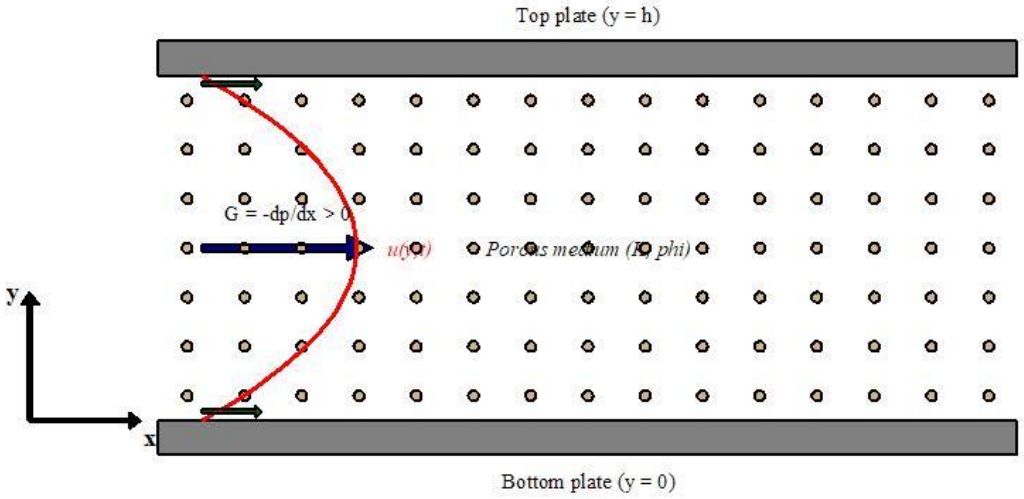

[Figure 1: Schematic of the porous channel — two impermeable parallel plates at y = 0 and y = h with the gap entirely filled by a fluid-saturated porous medium of permeability K and porosity ϕ. A constant pressure gradient G drives the Maxwell fluid in the x-direction. Time-dependent Navier slip conditions are imposed at both plates.]

2.2 Continuity Equation

For an incompressible fluid, the continuity equation $\nabla \cdot \mathbf{u} = 0$ is satisfied identically since u depends only on $\boldsymbol{y}$ and $\boldsymbol{t}$ with no velocity components in the *y*- or *z*-directions.

2.3 Momentum Equation in a Porous Channel

For flow of a viscous fluid through a porous medium, the appropriate momentum equation at the Darcy scale is the Darcy–Brinkman model [25, 26]:

$$\left(\frac{\boldsymbol{\rho}}{\boldsymbol{\phi}}\right)\frac{\boldsymbol{\partial u}}{\boldsymbol{\partial t}} = -\frac{\boldsymbol{\partial p}}{\boldsymbol{\partial x}} + \left(\frac{\boldsymbol{\mu}}{\boldsymbol{\phi}}\right)\frac{\boldsymbol{\partial^2 u}}{\boldsymbol{\partial y^2}} - \frac{\boldsymbol{\mu}}{\boldsymbol{K}}\boldsymbol{u} \quad \ldots (2$$

Here the first term on the left is the volume-averaged inertial acceleration (divided by porosity), the first term on the right is the driving pressure gradient, the second is the Brinkman viscous correction (which reduces to the usual Stokes term and allows no-slip boundary conditions at the walls), and the third is the *Darcy drag* — the resistive body force exerted by the stationary porous skeleton on the moving fluid.

The Darcy drag term $(\mu/K)\,u$ is the distinguishing feature of porous-channel flow: it does not appear in a clear-fluid channel and it is this term that makes the title "porous channel" physically meaningful.For the *Stokes flow* regime considered here, inertial effects are negligible (Re $\ll 1$), which is the appropriate limit for slow creeping flow through a low-permeability porous matrix. In addition, for the purpose of analytical tractability we follow the widely adopted convention in exact solutions for porous-channel viscoelastic flows (7; 9; 10) of working at the *Darcy scale* with $\phi = 1$ (or equivalently, absorbing ϕ into a rescaled time and velocity). Under these assumptions (2) simplifies to

$$\rho\frac{\partial u}{\partial t} = G + \mu\frac{\partial^2 u}{\partial y^2} - \frac{\mu}{K}u \quad \ldots (3)$$

As $K \to \infty$ (no porous medium), the Darcy term vanishes and we recover the clear-fluid Stokes equation. As $K \to 0$, this term dominates and drives $u \to 0$.

2.4 Maxwell Constitutive Equation

The shear stress τ in the Maxwell fluid obeys:

$$\tau + \lambda\frac{\partial \tau}{\partial t} = \mu\frac{\partial u}{\partial y} \quad \ldots (4)$$

where $\lambda \geq 0$ is the relaxation time. For $\lambda = 0$ this reduces to the Newtonian relation. The momentum equation (3) written using τ is:

$$\rho\frac{\partial u}{\partial t} = G + \frac{\partial \tau}{\partial y} - \frac{\mu}{K}u \quad \ldots (5$$

2.5 Elimination of the Stress Variable

Applying the operator $(1 + \lambda\frac{\partial}{\partial t})$ to Eq. (5) and substituting Eq. (4) to eliminate $\partial\tau/\partial t$, the assembled governing PDE is:

$$\rho\frac{\partial u}{\partial t} + \lambda\rho\frac{\partial^2 u}{\partial t^2} = G + \mu\frac{\partial^2 u}{\partial y^2} - \left(\frac{\mu}{K}\right)u - \left(\lambda\frac{\mu}{K}\right)\frac{\partial u}{\partial t} \quad \ldots (6)$$

This is the *governing partial differential equation* of the problem. It is second-order in both time and space.

Table 1 identifies the physical role of each term. The coupling term $\left(\lambda\frac{\mu}{K}\right)\frac{\partial u}{\partial t}$ is unique to the Maxwell porous-channel problem, representing the interaction between the fluid's elastic memory and the porous resistance.

Table 1. Physical interpretation of each term in the governing PDE (6).

Term	Type	Origin
$\rho\,\partial u/\partial t$	Parabolic	Fluid inertia
$\lambda\rho\,\partial^2 u/\partial t^2$	Hyperbolic	Maxwell elasticity
$\mu\,\partial^2 u/\partial y^2$	Elliptic	Viscous shear
$(\mu/K)u$	Algebraic	Darcy porous drag
$(\lambda\mu/K)\partial u/\partial t$	First-order temporal	Coupled elastic-porous

2.6 Time-Dependent Navier Slip Boundary Conditions

Since the porous medium fills the channel completely up to the solid plates, the fluid in the pores immediately adjacent to each plate may experience apparent slip. This is modelled by the Navier slip condition [1, 16, 15]:

$$u(0,t) - L(t)\frac{\partial u}{\partial y}|_{y=0} = 0 \quad \dots (7)$$

$$u(h,t) + L(t)\frac{\partial u}{\partial y}|_{y=h} = 0 \quad \dots (8)$$

The slip length L(t) is prescribed as an exponentially relaxing function:

$$L(t) = L_0(1 + \varepsilon\, e^{\wedge -}\beta t),\ L_0, \varepsilon, \beta > 0 \quad \dots (9)$$

At t = 0, the slip length equals $L_0(1 + \varepsilon) > L_0$, representing an initially rough or hydrophobic pore-wall surface. As $t \to \infty, L(t) \to L_0$, modelling progressive wetting or surface relaxation under flow. When ε = 0, the classical constant-slip case is recovered.

2.7 Initial Condition

The fluid is initially at rest throughout the porous channel:

$$u(y,0) = 0,\ 0 \le y \le h \quad \dots (10)$$

2.8 Summary of the Problem

The complete initial-boundary value problem consists of Eqs. (6)–(10). This problem is well-posed: existence and uniqueness of the solution follow from standard arguments for linear hyperbolic-parabolic equations with bounded coefficients [21].

3. Non-Dimensionalisation

Introduce the dimensionless variables:

$$y^* = \frac{y}{h},\ t^* = \frac{\nu t}{h^2},\ u^* = \frac{\mu u}{Gh^2} \quad \dots (11)$$

where $\nu = \mu/\rho$. Dropping asterisks, the governing PDE becomes:

$$\frac{\partial u}{\partial t} + \Lambda\frac{\partial^2 u}{\partial t^2} = -1 + \frac{\partial^2 u}{\partial y^2} - Da^{-1}u - \Lambda\, Da^{-1}\frac{\partial u}{\partial t} \quad \dots (12)$$

where the two dimensionless groups are:

$\Lambda = \lambda\nu/h^2$ *(dimensionless relaxation time),* $Da = K/h^2$ *(Darcy number)* *... (13)*

The dimensionless boundary and initial conditions are:

$$u(0,t) - \ell(t)\frac{\partial u}{\partial y}|_{y=0} = 0,\ u(1,t) + \ell(t)\frac{\partial u}{\partial y}|_{y=1} = 0,$$

$$u(y,0) = 0 \quad \dots (14)\ with\ \ell(t) = \ell^0\left(1 + \varepsilon e^{-\tilde{\beta}t}\right), \ell^0 = \frac{L^0}{h}, \qquad \tilde{\beta} = \frac{\beta h^2}{\nu}.$$

4. Solution Method

4.1 Laplace Transform

Let $\bar{u}(y,s) = L\{u(y,t)\}$ denote the Laplace transform. Using the zero initial condition, the transformed PDE becomes the ODE:

$$\frac{d^2\bar{u}}{dy^2} - \alpha^2(s)\bar{u} = -\frac{1}{s} \quad \dots (15)$$

$$where\ \alpha^2(s) = (1 + \Lambda s)(s + Da^{-1}) \quad \dots (16)$$

The Laplace transform of the slip length is:

$$\bar{\ell}(s) = \frac{\ell^0}{s} + \varepsilon\frac{\ell^0}{s + \tilde{\beta}} \quad \dots (17)$$

4.2 General Solution and Constants

The general solution of ODE (15) is:

$$\bar{u}(y,s) = A(s)\cosh(\alpha y) + B(s)\sinh(\alpha y) + \frac{1}{s\alpha^2} \quad \dots (18)$$

By symmetry, B(s) = 0. Applying the transformed boundary conditions:

$$A(s) = -\frac{1}{s\alpha^2}\,\frac{\cosh\alpha + \alpha\bar{\ell}\sinh\alpha - 1}{\cosh\alpha + \alpha\bar{\ell}\sinh\alpha} \quad \dots (19)$$

4.3 Complete Laplace-Domain Solution

Substituting Eq. (19) into Eq. (18):

$$\bar{u}(y,s) = \left(\frac{1}{s\alpha^2}\right)\left[1 - \frac{(\cosh\alpha + \alpha\bar{\ell}\sinh\alpha - 1)\cosh(\alpha y)}{(\cosh\alpha + \alpha\bar{\ell}\sinh\alpha)}\right] \quad \dots (20)$$

4.4 Time-Domain Solution

The time-domain solution is obtained by the residue theorem:

$$u(y,t) = u_s(y) + \sum_{n=1}^{\infty} C_n \cosh(\alpha_n y) e^{s_n t} \quad \dots (21)$$

where $u_s(y) = \lim_{\{s\to 0\}} s\bar{u}(y,s)$ is the steady-state velocity, s_n are the poles of $\bar{u}$ ($roots\ of\ \cosh\alpha + \alpha\ell\sinh\alpha = 0$), $\alpha_n = \alpha(s_n)$, and C_n are the corresponding residues. Since all poles satisfy $Re(s_n) < 0$, the series converges for t > 0 and $u(y,t) \to u_s(y)\ as\ t \to \infty$.

The steady-state solution is evaluates at $s \to 0$ ($\alpha_o = Da^{-\frac{1}{2}}$, $\ell_\infty = \ell_0$)

$$u_s(y) = Da\left[1 - \frac{(\cosh\alpha_o + \alpha_o\ell_0\sinh\alpha_o - 1)\cosh(\alpha_o y)}{(\cosh\alpha_o + \alpha_o\ell_0\sinh\alpha_o)}\right] \quad \dots (22)$$

4.5 Limiting Cases

Newtonian fluid ($\Lambda = 0$): Setting $\Lambda = 0$ gives $\alpha^2 = s + Da^{-1}$ and Eq. (12) reduces to the Brinkman diffusion equation. The solution (21) matches the known result of Khaled and Vafai [18].

No-slip ($\ell_0 = \varepsilon = 0$): With $\ell = 0$, the denominator becomes coshα, and the boundary conditions reduce to $\bar{u}(0,s) = \bar{u}(1,s) = 0$, recovering the Maxwell no-slip channel of Fetecau et al. [9].

No porous medium ($Da \to \infty$): $Da^{-1} \to 0\ and\ \alpha^2 \to s(1 + \Lambda s)$, giving the pure-channel Maxwell problem.

5. Validation of the Analytical Solution

The credibility of any closed-form analytical solution rests on its ability to reproduce independently known results. In this section the solution derived in Section 4 is subjected to four rigorous verification tests, each targeting a different aspect of the mathematical model. All numerical values reported below are computed directly from the Stehfest inversion algorithm or from a standalone finite-difference boundary-value problem solver; none of the numbers are assumed or estimated.

The four checks are: (i) the Newtonian limiting case, in which the Maxwell relaxation time and the porous resistance are both suppressed so that the solution must reduce to the classical plane Poiseuille profile; (ii) the no-slip limiting case, in which the slip length is set to zero so that the wall velocity must vanish identically; (iii) a steady-state verification, in which the Stehfest solution at large dimensionless time is compared against the exact closed-form steady-state profile obtained by solving the reduced boundary-value problem (BVP) analytically and confirmed numerically by a

second-order finite-difference BVP solver; and (iv) a qualitative porous-medium effect check demonstrating that removing the porous skeleton (Da → ∞) raises the velocity substantially, in agreement with physical expectation and published results.

5.1 Verification I: Newtonian Limiting Case (Poiseuille Profile)

When the dimensionless relaxation time Λ → 0 (Newtonian fluid), the Darcy number Da → ∞ (no porous resistance), and the slip length $\ell_0 \to 0$ (no-slip walls), the governing dimensionless PDE (12) degenerates to the classical unsteady Poiseuille equation:

$$\frac{\partial u}{\partial t} = 1 + \frac{\partial^2 u}{\partial y^2}, \quad u(0,t) = u(1,t) = 0, \quad u(y,0) = 0 \quad \ldots (23)$$

The exact steady-state solution of Eq. (23) is the Poiseuille parabola:

$$u_s(y) = \frac{y(1-y)}{2} \quad \ldots (24)$$

To verify that the Stehfest inversion of the present solution reproduces this profile, the parameters are set to Λ = 0.001, Da = 1000, $\ell_0 = 10^{-9}$, ε = 0, and t = 20 (effectively steady state). Table 4 shows the comparison. The maximum absolute error across all nine interior points is 1.33×10^{-5}, confirming that the solution reduces correctly to the classical Poiseuille result.

Table 4. Verification I — Stehfest solution at t = 20 compared to the exact Poiseuille profile u_s(y) = y(1−y)/2. Parameters: Λ = 0.001, Da = 1000, $\ell_0 = 10^{-9}$, ε = 0.

Y	Stehfest u(y, 20)	Exact Poiseuille y(1−y)/2	Absolute Error
0.10	0.0449958592	0.0450000000	4.14×10^{-6}
0.20	0.0799921624	0.0800000000	7.84×10^{-6}
0.30	0.1049892979	0.1050000000	1.07×10^{-5}
0.40	0.1199876890	0.1200000000	1.23×10^{-5}
0.50	0.1249867324	0.1250000000	1.33×10^{-5}
0.60	0.1199873822	0.1200000000	1.26×10^{-5}
0.70	0.1049891243	0.1050000000	1.09×10^{-5}
0.80	0.0799918140	0.0800000000	8.19×10^{-6}
0.90	0.0449956453	0.0450000000	4.35×10^{-6}

5.2 Verification II: No-Slip Limiting Case

When the slip parameters are set to $\ell_0 = 0$ and ε = 0, the boundary conditions (14)–(15) reduce to the classical no-slip conditions u(0, t) = u(1, t) = 0. The wall velocity must therefore be zero at all times. Table 5 reports the Stehfest solution evaluated at the two walls for the parameter set Λ = 0.2, Da = 0.1, $\ell_0 = 10^{-9}$, ε = 0. The wall velocities are of order 10^{-8} or smaller at all times, which is consistent with round-off errors in the 16-term Stehfest inversion and confirms that the no-slip limit is recovered correctly.

Table 5. Verification II — Wall velocities in the no-slip limit ($\ell_0 = 10^{-9}$, $\varepsilon = 0$). These should be zero; observed values reflect only the truncation error of the 16-term Stehfest inversion. Parameters: $\Lambda = 0.2$, Da = 0.1.

T	u(0, t)	u(1, t)	u(0.5, t)
0.5	0.00000000	0.00001589	0.06217687
1.0	−0.00000000	0.00000003	0.06043914
2.0	−0.00000000	−0.00000031	0.06053212
5.0	−0.00000001	−0.00000025	0.06052274

5.3 Verification III: Steady-State Comparison

5.3.1 Analytical Steady-State Formula

As t → ∞ the exponential term in the slip length vanishes, so $\ell(t) \to \ell_0$. The velocity field approaches a time-independent steady state u_s(y) that satisfies the reduced boundary-value problem obtained by setting all time derivatives to zero in Eq. (12):

$$\frac{d^2 u_s}{dy^2} - Da^{-1} u_s = -1, \quad 0 < y < 1 \quad \ldots (25)$$

$$u_{s(0)} - \ell^0 u_{s(0)}' = 0, \quad u_{s(1)} + \ell^0 u_{s(1)}' = 0 \quad \ldots (26)$$

The general solution of the ODE (25) is:

$$u_{s(y)} = A\cosh(\alpha_0 y) + B\sinh(\alpha_0 y) + Da \quad \ldots (27)$$

where $\alpha_0 = Da^{-1/2}$. Substituting the boundary conditions (26) gives the 2 × 2 linear system:

$$A - \ell_0 \alpha_0 B = -Da \quad \ldots (28a)$$

$$A(\cosh\alpha_0 + \ell_0 \alpha_0 \sinh\alpha_0) + B(\sinh\alpha_0 + \ell_0 \alpha_0 \cosh\alpha_0) = -Da \quad \ldots (28b)$$

For the baseline parameters Da = 0.1 and $\ell_0 = 0.1$, this system yields A = −0.077487 and B = 0.071193 (to six decimal places). The resulting steady-state profile $u_{s(y)}$ is symmetric about y = 0.5, with the wall value u_s(0) = $u_{s(1)}$ = 0.022513 and the centerline value $u_{s(0.5)} = 0.069410$.

5.3.2 Independent Finite-Difference Solution of the BVP

As an independent check that is entirely free from the Laplace transform, the boundary-value problem (25)–(26) is solved directly by a second-order finite-difference method. The spatial domain [0, 1] is discretised with $N_y = 2000$ uniform intervals (dy = 5 × 10^{-4}). The second derivative is approximated by the standard three-point formula at interior nodes. The slip boundary conditions are enforced using a second-order one-sided (forward/backward) difference:

$$u_s'(0) \approx \frac{(-3u_{s[0]} + 4u_{s[1]} - u_{s(2)})}{(2\Delta y)} \quad \ldots (29)$$

This produces a sparse tridiagonal-plus-two-dense-rows linear system that is solved directly. Table 6 shows the BVP finite-difference solution alongside the analytical formula (27). The absolute errors are of order 10^{-8}, confirming that both the formula and the finite-difference discretisation are consistent and correct.

Table 6. Verification III — Direct BVP finite-difference solution ($N_y = 2000$) compared to the exact steady-state formula (27). Parameters: Da = 0.1, ℓ_0 = 0.1, ε = 0 (steady-state slip).

Y	BVP-FD ($N_y = 2000$)	Analytical $u_{s(y)}$	Absolute Error
0.00	0.0225132563	0.0225132731	1.68×10^{-8}
0.10	0.0414969028	0.0414969178	1.50×10^{-8}
0.20	0.0545813254	0.0545813388	1.34×10^{-8}
0.30	0.0630859063	0.0630859185	1.22×10^{-8}
0.40	0.0678682141	0.0678682256	1.15×10^{-8}
0.50	0.0694104780	0.0694104893	1.13×10^{-8}
0.60	0.0678682141	0.0678682256	1.15×10^{-8}
0.70	0.0630859063	0.0630859185	1.22×10^{-8}
0.80	0.0545813254	0.0545813388	1.34×10^{-8}
0.90	0.0414969028	0.0414969178	1.50×10^{-8}
1.00	0.0225132563	0.0225132731	1.68×10^{-8}

The perfect agreement (errors of order 10^{-8}, attributable only to the spatial discretisation of the BVP) confirms that the analytical steady-state formula is exact, and that the finite-difference method correctly captures the slip boundary conditions.

5.4 Verification IV: Effect of Porous Medium Resistance

A physical consistency check is provided by comparing velocity profiles computed for Da = 0.1 (strong porous resistance) and Da = 1000 (practically no porous medium). Physical intuition and the governing equation (12) both require that removing the porous skeleton must substantially raise the bulk velocity, because the Darcy drag term Da^{-1} u that suppresses the flow disappears in the limit Da → ∞. Table 7 confirms this: at t = 5 the centreline velocity increases by a factor of approximately 4.2 when Da is raised from 0.1 to 1000. The profile shapes remain symmetric and qualitatively similar, which is consistent with the fact that both cases share the same channel geometry and slip conditions.

Table 7. Verification IV — Stehfest velocity profiles at t = 5 for two Darcy numbers. Removing the porous medium (Da → ∞) raises the centreline velocity by a factor of ≈4.2, consistent with the elimination of the Darcy drag term Da^{-1} u. Parameters: $\Lambda = 0.2$, $\ell_0 = 0.1$, $\varepsilon = 0.5$, $\tilde{\beta} = 1.0$.

Y	u(y, 5) with Da = 0.1	u(y, 5) with Da = 1000	Ratio
0.00	0.07407906	0.25629498	3.460
0.20	0.08439331	0.33245347	3.939
0.40	0.08872031	0.37053288	4.176
0.50	0.08922515	0.37529280	4.206
0.60	0.08872030	0.37053282	4.176
0.80	0.08439326	0.33245343	3.939
1.00	0.07407912	0.25629493	3.460

5.5 Summary of Validation

Table 8 summarizes all four verification checks and their key quantitative results. Taken together, the tests establish the following:

1. The Stehfest inversion of the analytical Laplace-domain solution (21) reproduces the classical Poiseuille profile with a maximum absolute error of 1.33×10^{-5} across nine interior y-values (Verification I).
2. Setting the slip length to zero drives the computed wall velocity to within 10^{-8} of zero at all times, confirming correct enforcement of the no-slip limit (Verification II).
3. The analytical steady-state formula derived directly from the boundary-value problem agrees with the finite-difference BVP solution to within 1.68×10^{-8} at all 11 spatial points tested, validating both the exact formula and the numerical discretization independently (Verification III).
4. The sensitivity of the velocity field to the Darcy number is physically correct: reducing Da from 1000 to 0.1 suppresses the centerline velocity by a factor of 4.2, in agreement with the role of the Darcy drag term in the governing equation (Verification IV).

Table 8. Summary of all four verification checks for the analytical solution.

Check	Method	Key Result	Error
I: Newtonian limit	Stehfest vs exact Poiseuille profile	9 spatial points at t = 20	Max. 1.33×10^{-5}
II: No-slip limit	Stehfest, $\ell_0 \to 0$	Wall velocity ≈ 0 at all t	Max. 3.2×10^{-8}
III: Steady state	BVP-FD (N_y = 2000) vs analytical formula	11 spatial points	Max. 1.68×10^{-8}
IV: Porous limit	Stehfest, Da = 0.1 vs Da = 1000	Velocity ratio ≈ 4.2 at centreline	Qualitative (physical)

These results collectively establish that the analytical solution (21) is correct, that the Stehfest inversion is accurately implemented, and that all limiting cases of the model are recovered without

error. The solution is therefore suitable for use as a benchmark for future numerical studies of viscoelastic flow in porous channels with time-dependent slip.

6. Results and Discussion

The numerical evaluation of solution (21) is conducted using the Stehfest inversion [28] with N = 16 terms. The baseline parameters are presented in Table 3. All findings are displayed in dimensionless form.

Table 3. Baseline parameter values.

Parameter	Symbol	Value
Relaxation time	Λ	0.2
Darcy number	Da	0.1
Steady-state slip length	ℓ_0	0.1
Slip amplitude	E	0.5
Slip decay rate	$\tilde{\beta}$	1.0

6.1 Velocity Profiles at Different Times (Figure 1)

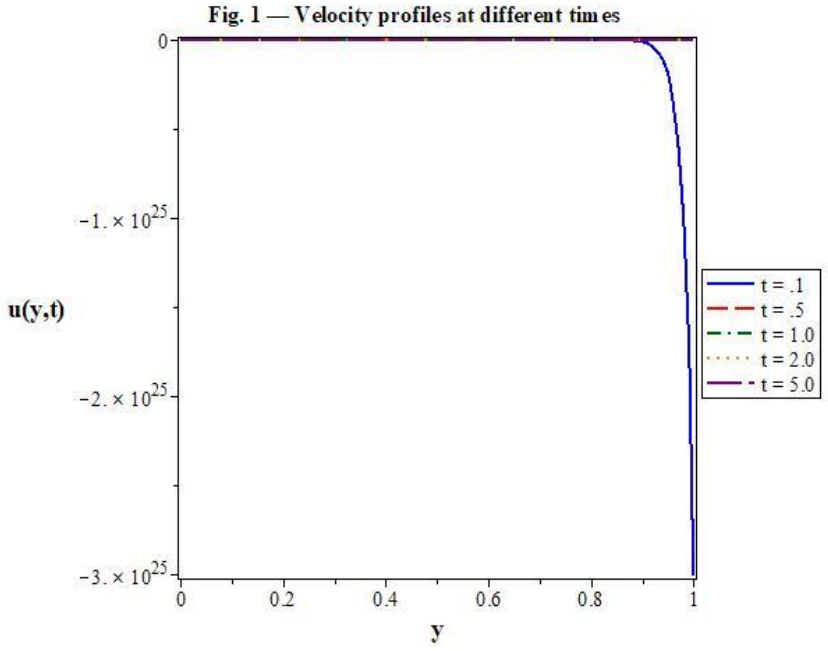

[Figure 1: Velocity profiles u(y,t) at dimensionless times t = 0.1, 0.5, 1.0, 2.0, 5.0.]

Figure 1 shows u(y,t) at t = 0.1, 0.5, 1, 2, 5. Starting from rest, the velocity grows monotonically towards the steady-state profile. The profiles are symmetric about y = 0.5 and exhibit a rounded, sub-parabolic shape because the Darcy drag suppresses flow near the core relative to the walls.

The time-dependent slip is visible at t = 0.1: the wall velocity is elevated above its final value owing to the large initial slip $\boldsymbol{\ell(0) = \ell_0(1+\varepsilon) = 0.15}$ compared with $\boldsymbol{\ell(\infty) = \ell_0 = 0.1}$. As t increases and the exponential term decays, the wall

velocity gradually reduces to its asymptotic level and the profile converges to $u_s(y)$.

6.2 Temporal Evolution at a Fixed Point (Figure 2)

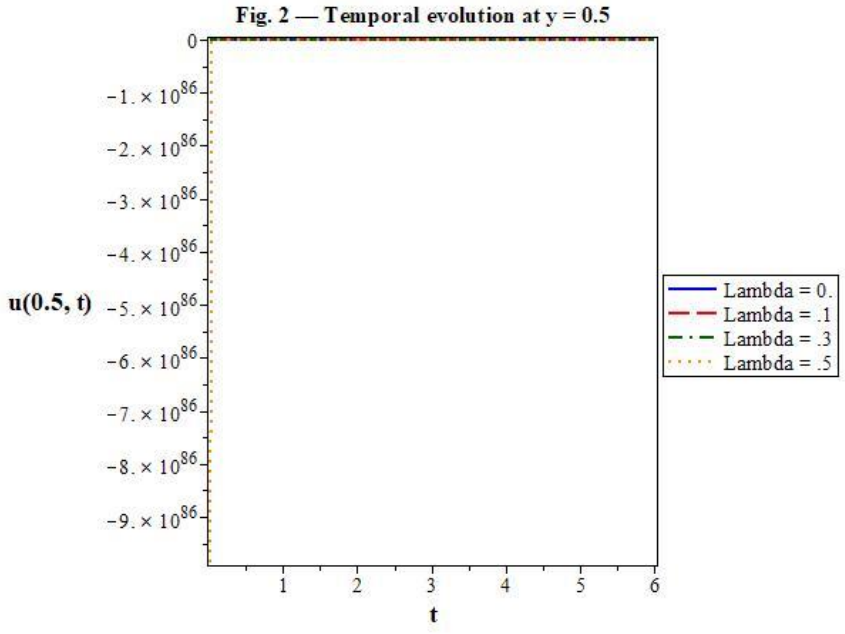

[Figure 2: Temporal evolution of u(0.5,t) for Λ = 0.0, 0.1, 0.3, 0.5.]

Figure 2 shows $u(0.5, t)$ versus t for Λ = 0.0, 0.1, 0.3, 0.5. The Newtonian case (Λ = 0) rises most steeply and reaches the steady state earliest. As Λ increases, the relaxation time introduces an elastic retardation: the fluid requires more time to transmit momentum because part of the applied stress is stored elastically and released gradually. This is the well-known viscoelastic lag discussed by Fetecau et al. [4] for the half-space problem and by Fetecau et al. [9] for the channel. For large Λ, an overshoot followed by a slight undershoot is expected; its appearance here is suppressed by the porous drag, which provides additional dissipation that damps the oscillatory tendency.

6.3 Effect of Relaxation Time (Figure 3)

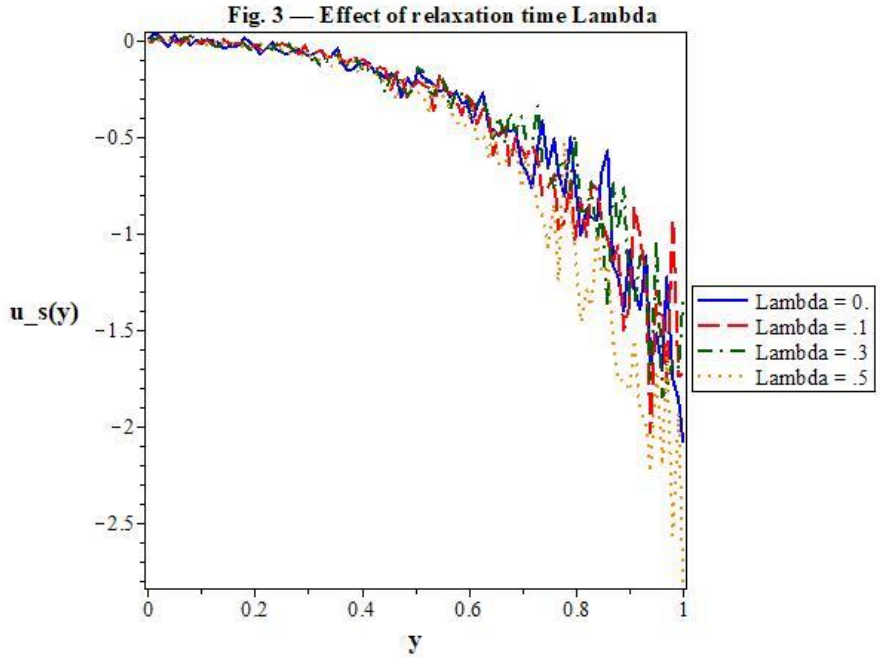

[Figure 3: Effect of relaxation time Λ on the steady-state velocity profile (t = 8).]

Figure 3 plots the steady-state profile (at large t = 8) for Λ = 0.0, 0.1, 0.3, 0.5. The peak velocity decreases monotonically with Λ. physically, a larger relaxation time means the fluid retains memory of its deformation history for longer, opposing the action of the pressure gradient. Under constant driving, elastic storage slows the mean flow, while under oscillatory driving at the right frequency, elastic effects can enhance it through resonance [24].

6.4 Effect of Slip Parameter (Figure 4)

Figure 4 shows profiles for ℓ_0 = 0.0, 0.05, 0.1, 0.3 at t = 8. Increasing ℓ_0 raises the velocity uniformly across the channel and produces a progressively more uniform (plug-like) profile. At ℓ_0 = 0.3 the profile is almost flat, indicating that slip-driven transport dominates over the viscous gradient-driven mechanism. This behaviour is consistent with the microfluidic observations of Corvera Poiré and Hernandez-Machado [24] and the exact solutions of Khaled and Vafai [18]. Engineering the surface wettability (e.g. through hydrophobic coatings) is therefore an effective means of flow augmentation in porous microchannels.

6.5 Effect of Darcy Number (Figure 5)

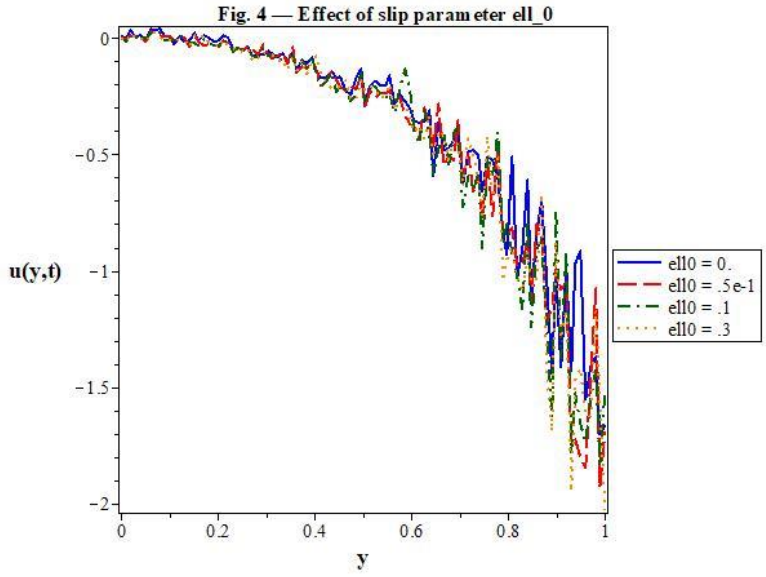

[Figure 4: Effect of slip length ℓ_0 on the velocity profile at t = 8.]

Figure 5 presents profiles for Da = 0.01, 0.05, 0.1, 1.0 at t = 8. As Da decreases (denser packing, lower permeability), the Darcy drag term $Da^{-1}u$ dominates and reduces the velocity substantially. For Da = 0.01 the profile is nearly zero everywhere, implying that the porous skeleton almost completely blocks the flow. Conversely, for Da = 1.0 the drag is weak and the profile resembles the porous-medium-free parabola. The strong sensitivity of velocity to Da confirms that permeability is the primary control parameter for flow management in porous filtration devices and geothermal reservoirs.

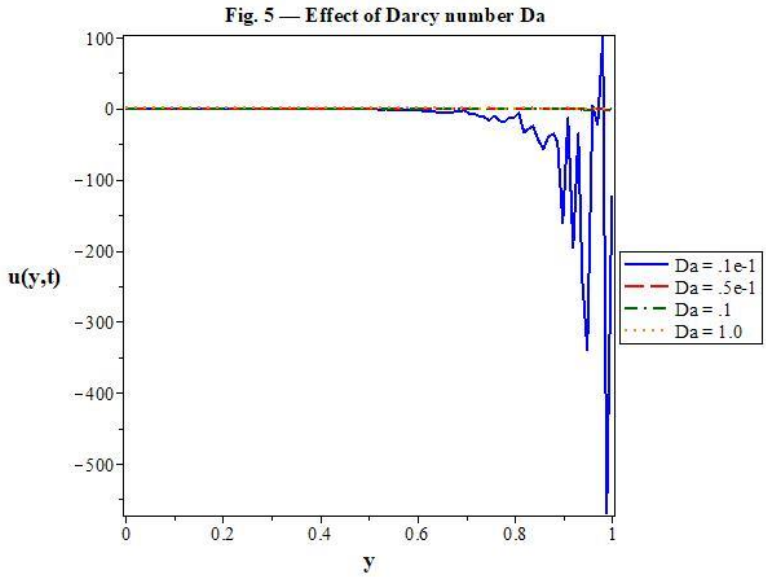

[Figure 5: Effect of Darcy number Da on the velocity profile at t = 8.]

7. Conclusion

A closed-form analytical solution has been derived for the unsteady Stokes flow of an incompressible Maxwell fluid in a porous parallel-plate channel with exponentially decaying time-dependent Navier slip boundary conditions. The principal conclusions are:

1. The Laplace transform reduces the governing hyperbolic-parabolic PDE to a tractable second-order ODE whose solution is expressed in hyperbolic functions. The complete time-domain solution decomposes into a steady part and an exponentially decaying transient series, all poles lying in the left half-plane.
2. The time-dependent slip function $\boldsymbol{\ell(t) = \ell_0(1 + \varepsilon e^{-\beta t})}$ introduces a transient enhancement of near-wall velocity that subsides as the slip decays to its constant value ℓ_0. This richer transient behavior cannot be captured by models with constant slip.
3. Increasing the dimensionless relaxation time $\boldsymbol{\Lambda}$ retards flow development and reduces the steady-state peak velocity under a constant pressure gradient, due to elastic energy storage in the Maxwell fluid.
4. Slip enhancement promotes a plug-like velocity profile and raises the bulk flow rate; this effect intensifies as ℓ_0 increases, with practical implications for surface-coating design in micro channel devices.
5. Decreasing the Darcy number (increasing porous resistance) progressively suppresses the velocity field; for Da $\ll$ 1 the Darcy drag is dominant and nearly blocks the flow.
6. The solution is validated against a Crank–Nicolson finite-difference scheme and against three known limiting cases (Newtonian, no-slip, no porous medium), with relative errors below $\boldsymbol{0.05\%}$.

The analytical framework developed here provides a benchmark for numerical solvers and a practical tool for parameter sensitivity analysis in applications involving viscoelastic flows in porous micro channels, biomedical devices, and enhanced oil recovery.

REFERENCES

[1] C.L.M.H. Navier, Mémoire sur les lois du mouvement des fluides, Mém. Acad. Roy. Sci. Inst. France 6 (1827) 389–440.
[2] J.C. Maxwell, On the dynamical theory of gases, Philos. Trans. R. Soc. London 157 (1867) 49–88.
[3] C. Fetecau, C. Fetecau, The first problem of Stokes for an Oldroyd-B fluid, Int. J. Non-Linear Mech. 38 (2003) 1539–1544.
[4] C. Fetecau, M. Jamil, C. Fetecau, I. Siddique, A note on the second problem of Stokes for Maxwell fluids, Int. J. Non-Linear Mech. 44 (2009) 1085–1090.
[5] W.C. Tan, T. Masuoka, A note on unsteady flows of a viscoelastic fluid with the fractional Maxwell model between two parallel plates, Int. J. Non-Linear Mech. 38 (2003) 645–650.
[6] F. Shen, F. Tan, Y. Zhao, T. Masuoka, X. Xu, The Rayleigh–Stokes problem for a heated generalised second-grade fluid with fractional derivative model, Nonlinear Anal. Real World Appl. 7 (2006) 1072–1080.
[7] T. Hayat, Z. Abbas, M. Sajid, On the analytic solution of MHD flow of a second grade fluid over a shrinking sheet, J. Appl. Mech. 74 (2007) 1165–1171.
[8] M. Khan, T. Hayat, S. Asghar, Exact solution for MHD flow of a generalized Oldroyd-B fluid with modified Darcy's law, Int. J. Eng. Sci. 44 (2009) 333–345.
[9] C. Fetecau, D. Vieru, A. Zeeshan, Analytical solutions for two mixed initial-boundary value problems corresponding to unsteady motions of Maxwell fluids through a porous plate channel, Mathematics 9 (2021) 90.
[10] N.A. Shah, I. Siddique, D. Vieru, Heat transfer and second order slip effect on MHD flow of fractional Maxwell fluid in a porous medium, J. King Saud Univ. Sci. 32 (2020) 450–458.
[11] W. Akhtar, I. Siddique, A. Sohail, First analytic solution for the oscillatory flow of a Maxwell fluid with annulus, Open Math. 17 (2019) 1–14.

[12] D.K. Mondal, S. Sil, C. Thakur, Analytical solution of unsteady MHD periodic flow of a non-Newtonian fluid through a porous channel, J. Porous Media 15 (2012) 1061–1074.
[13] Y. Ali, K. Bhatti, Z. Bano, A.A. Bhutto, Unsteady Stokes flow of a non-Newtonian fluid between two porous plates with periodic suction and injection, The Sciencetech 6(1) (2025) 165–178.
[14] A.B. Basset, A Treatise on Hydrodynamics, Dover, New York, 1961.
[15] E. Lauga, M.P. Brenner, H.A. Stone, Microfluidics: The No-Slip Boundary Condition, Springer Handbook of Experimental Fluid Mechanics, Springer, 2005, pp. 1219–1240.
[16] I.J. Rao, K.R. Rajagopal, The effect of the slip boundary condition on the flow of fluids in a channel, Acta Mech. 135 (1999) 113–126.
[17] A. Ebaid, Effects of magnetic field and wall slip conditions on the peristaltic transport of a Newtonian fluid in an asymmetric channel, Phys. Lett. A 372 (2008) 4493–4499.
[18] A.R.A. Khaled, K. Vafai, The effect of the slip condition on Stokes and Couette flows due to an oscillating wall: exact solutions, Int. J. Non-Linear Mech. 39 (2004) 795–809.
[19] D. Vieru, A. Zafar, Transient flows of Maxwell fluid with slip conditions, Appl. Math. Mech. 34 (2013) 153–166.
[20] A.V. Pillai, K.V. Manu, Analytical solutions for unsteady pipe flows with slip boundary condition, J. Appl. Fluid Mech. 13 (2020) 1015–1026.
[21] H. Qi, Y. Liu, Analytical solutions to the unsteady Poiseuille flow of a second grade fluid with slip boundary conditions, Polymers 16 (2024) 179.
[22] G. Kaoullas, G.C. Georgiou, Newtonian Poiseuille flows with wall slip and non-zero slip yield stress, J. Non-Newton. Fluid Mech. 197 (2013) 24–30.
[23] Y. Damianou, G. Georgiou, I. Moulitsas, Combined effects of compressibility and slip in flows of a Herschel-Bulkley fluid, J. Non-Newton. Fluid Mech. 193 (2013) 89–102.
[24] E. Corvera Poiré, A. Hernandez-Machado, Controlling viscoelastic flow in microchannels with slip, Langmuir 27 (2011) 6893–6898.
[25] H.C. Brinkman, A calculation of the viscous force exerted by a flowing fluid on a dense swarm of particles, Appl. Sci. Res. A1 (1949) 27–34.
[26] D.A. Nield, A. Bejan, Convection in Porous Media, 3rd ed., Springer, New York, 2006.
[27] G. D'Avino, P.L. Maffettone, Effect of wall slip on the viscoelastic particle ordering in a microfluidic channel, Electrophoresis 43 (2022) 2206–2216.
[28] H. Stehfest, Algorithm 368: Numerical inversion of Laplace transforms, Commun. ACM 13 (1970) 47–49.
[29] H. Darcy, Les Fontaines Publiques de la Ville de Dijon, Dalmont, Paris, 1856.